MATERIALS SCIENCE

Millisecond lattice gasification for high-density CO_2- and O_2-sieving nanopores in single-layer graphene

Shiqi Huang[1], Shaoxian Li[1], Luis Francisco Villalobos[1], Mostapha Dakhchoune[1], Marina Micari[1], Deepu J. Babu[1], Mohammad Tohidi Vahdat[1], Mounir Mensi[2], Emad Oveisi[3], Kumar Varoon Agrawal[1]*

Etching single-layer graphene to incorporate a high pore density with sub-angstrom precision in molecular differentiation is critical to realize the promising high-flux separation of similar-sized gas molecules, e.g., CO_2 from N_2. However, rapid etching kinetics needed to achieve the high pore density is challenging to control for such precision. Here, we report a millisecond carbon gasification chemistry incorporating high density (>10^{12} cm^{-2}) of functional oxygen clusters that then evolve in CO_2-sieving vacancy defects under controlled and predictable gasification conditions. A statistical distribution of nanopore lattice isomers is observed, in good agreement with the theoretical solution to the isomer cataloging problem. The gasification technique is scalable, and a centimeter-scale membrane is demonstrated. Last, molecular cutoff could be adjusted by 0.1 Å by in situ expansion of the vacancy defects in an O_2 atmosphere. Large CO_2 and O_2 permeances (>10,000 and 1000 GPU, respectively) are demonstrated accompanying attractive CO_2/N_2 and O_2/N_2 selectivities.

INTRODUCTION

Molecular separation, a key component of industrial processes and at the heart of environmental issues such as carbon capture, is highly energy intensive (*1*). The energy efficiency and capital cost of the separation processes can be substantially reduced by using high-performance molecular-sieving membranes separating gases based on their kinetic diameters (*2*–*5*). Specifically, substantial improvement in energy efficiency of separation processes such as postcombustion carbon capture can be achieved by increasing the CO_2 permeance (*6*, *7*). Gas-sieving nanoporous single-layer graphene (N-SLG), prepared by incorporating vacancy defects in the SLG lattice (*8*, *9*), can be highly attractive for high-flux CO_2 and O_2 separation because the diffusion resistance is controlled by a single transition state at the nanopore (*10*–*13*).

While molecular simulations have predicted that graphene nanopores can indeed separate industrially relevant mixtures containing similar-sized molecules such as CO_2/N_2 (*14*), CO_2/CH_4 (*15*), O_2/N_2 (*16*), etc., it has remained challenging to incorporate these nanopores in graphene with a narrow-enough pore-size distribution (PSD) to obtain the needed sub-angstrom resolution in molecular differentiation (*17*–*19*). Furthermore, for developing practical membranes, the lattice transformation must take place uniformly over a macroscopically large area. The state-of-the-art etching methods have an inherent limitation; the pore expansion takes place at a much faster rate than that of pore nucleation. For example, the nanofabrication route, involving high-energy electron or ion bombardment, involves an energy barrier of 20 to 23 eV (*20*–*22*) to displace a carbon atom from the basal plane (nucleation event), much higher than that needed to displace a carbon atom from the pore edge (pore growth, ~14 eV) (*22*). Consequently, this limitation results in a broad PSD. We have shown that N-SLG with broad PSD can be used for gas separation, albeit using an additional gas-selective layer on top of graphene (*23*, *24*). Chemical etching technique involving O_2 (*8*, *25*), ultraviolet/O_3 (*17*), or O_3 (*19*, *26*), in principle, can obtain CO_2-selective nanopores by slowing down the etching kinetics, e.g., using a low temperature or a small concentration of etchant (*17*). However, approaches based on sluggish kinetics would not achieve the meaningful pore density needed to realize the primary objective of high-flux separation. Therefore, developing methods involving rapid etching kinetics coupled with short but controllable pore expansion time is critically needed. Here, by using a custom-made millisecond gasification reactor (MGR), we could control the expansion time of vacancy defects to a few milliseconds. High pore density (>10^{12} cm^{-2}) combined with a narrow PSD consisting of missing 1 to 20 carbon atoms led to attractive CO_2/N_2 and CO_2/CH_4 selectivities. The gasification technique is highly scalable and could be used to produce centimeter-scale N-SLG membranes. Furthermore, we show that molecular cutoff can be adjusted by 0.1 Å by a slow expansion of nanopores in situ inside the membrane module. The resulting membranes yielded attractive sieving performances with large CO_2 and O_2 permeances [>10,000 and 1000 gas permeation units (GPU), respectively], making these membranes highly promising for energy-efficient carbon capture.

RESULTS

Millisecond gasification of graphene

High-quality SLG (I_{2D}/I_G ratio of 4.8 ± 0.25) with a low density of intrinsic defects (I_D/I_G ratio of 0.04 ± 0.02) was synthesized by low-pressure chemical vapor deposition (LPCVD) (*27*) on an annealed Cu foil (*28*). Briefly, the Cu foils were thermally annealed to obtain Cu (111) to improve the uniformity of graphene and to reduce the density of intrinsic vacancy defects (fig. S1 and table S1) (*29*, *30*). The MGR is composed of an O_3 (etchant) supply to a hot chamber (120° to 290°C) via a millisecond leak valve (MLV) (Fig. 1, A and B, and fig. S2, A and B). To initiate the etching, the as-synthesized SLG was heated to the reaction temperature inside an evacuated MGR, and MLV was opened for 0.01 to 0.2 s, allowing a short O_3 pulse (full width at half maximum of 0.3 s; fig. S2C) with peak O_3 pressure

[1]Laboratory of Advanced Separations (LAS), École Polytechnique Fédérale de Lausanne (EPFL), 1950 Sion, Switzerland. [2]Institut des Sciences et Ingénierie Chimiques (ISIC), EPFL, 1950 Sion, Switzerland. [3]Interdisciplinary Centre for Electron Microscopy (CIME), EPFL, 1015 Lausanne, Switzerland.
*Corresponding author. Email: kumar.agrawal@epfl.ch

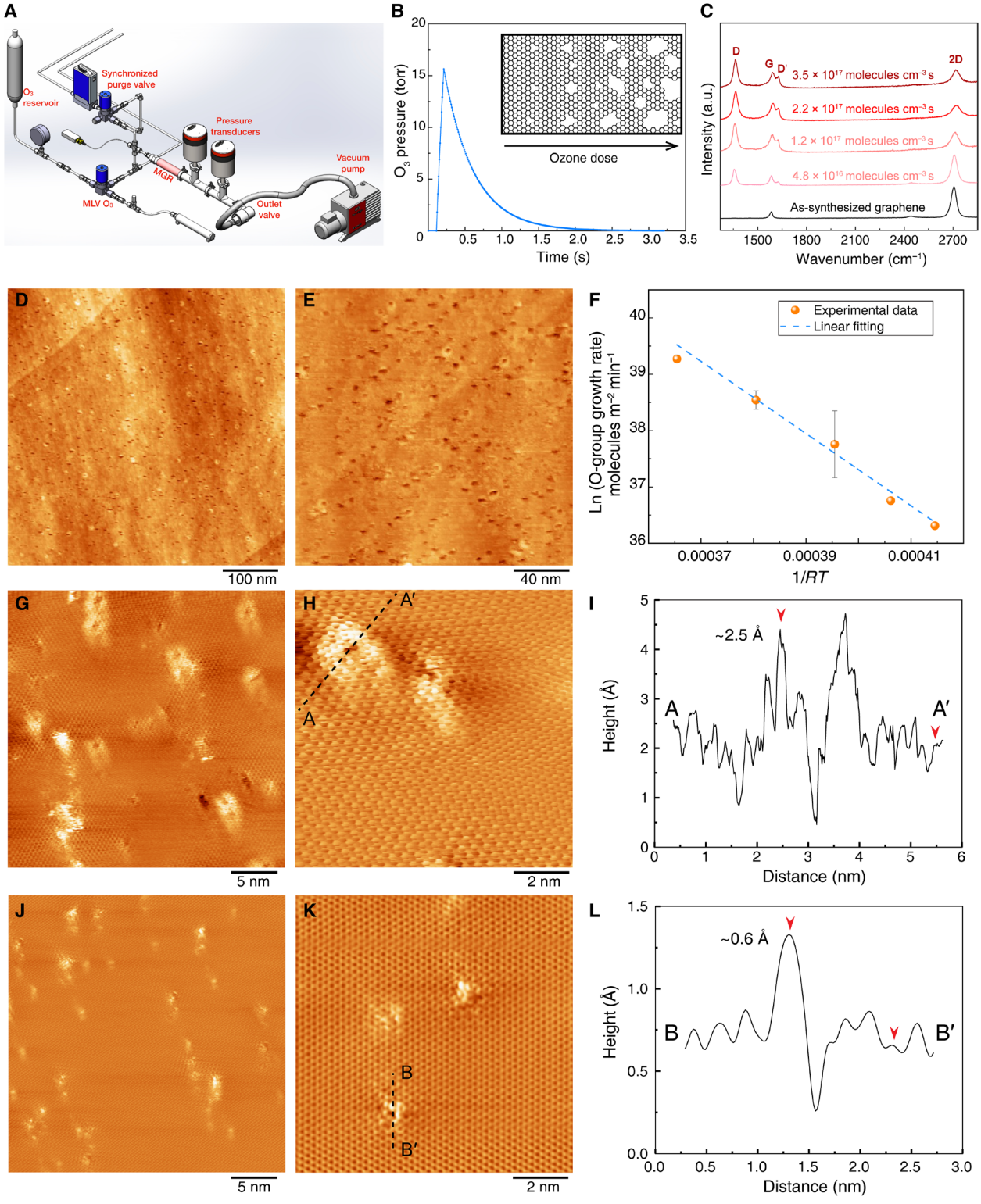

Fig. 1. Precise incorporation of a high density of vacancy defects in graphene by millisecond gasification. (**A**) Schematic of the MGR setup. (**B**) Profile of the O_3 pulse in MGR. (**C**) Raman spectroscopy analysis showing the evolution of the N-SLG with increasing O_3 dose. (**D** and **E**) Scanning tunneling microscopy (STM) images of N-SLG on Cu foil prepared by MGR at 250°C. The sample was annealed at 900°C before the STM imaging. (**F**) The temperature-dependent coverage rate of the functional oxygen groups on N-SLG fitted with linear regression. In the *x* axis, *R* refers to the universal gas constant and *T* refers to the functionalization temperature. (**G** and **H**) STM images of highly oriented pyrolytic graphite (HOPG) treated by MGR at 250°C. (**I**) The height profile of the line (AA′) in (H). The images were acquired by transferring samples to STM immediately after MGR, and no further thermal annealing was carried out. STM images of samples shown in (G and H) after annealing at 800°C inside the STM chamber (**J** and **K**). (**L**) The height profile of the line (BB′) in (K). a.u., arbitrary units.

in the range of 3 to 27 torr. The O_3 dose, calculated by the area under the curve of O_3 pressure as a function of time, was controlled by varying the MLV opening time (τ) and O_3 supply pressure (P_{up}) (table S2). Optionally, a purge (Ar or He) was opened after a synchronized delay time (t_d) to facilitate a rapid removal of O_3 (fig. S2D). Overall, O_3 dosage of 3.2×10^{16} to 3.5×10^{17} molecules cm^{-3} s was delivered while keeping the etching time well below 1 s (notes S1 and S2).

Raman spectroscopy of N-SLG films, exposed to increasing O_3 dose from 4.8×10^{16} to 3.5×10^{17} molecules cm^{-3} s, revealed significant D and D' peaks (Fig. 1C and fig. S3). The $I_D/I_{D'}$ ratios were well below 7. The maximum value was around 3, indicating that most of the defects were edge-like defects of graphite (*31*, *32*). I_D/I_G mapping indicated that the defects could be generated uniformly over a large area (fig. S3B).

Scanning tunneling microscopy (STM) was carried out directly on N-SLG, prepared by MGR (τ = 0.1 s, t_d = 0.5 s, and O_3 dosage of 1.6×10^{17} molecules cm^{-3} s), resting over the Cu foil without the need of transferring graphene to understand pore size, pore density, and their organization in the graphene lattice. The surface of Cu foil was partially oxidized during gasification, and therefore, to obtain a conductive and smooth surface for STM, N-SLG was annealed at 900°C in H_2. The corresponding STM images revealed that millisecond gasification led to a high density (~10^{12} cm^{-2}) of sub-nanometer vacancy defects (Fig. 1, D and E, and fig. S4). Several nanopores appeared to be aligned and were distributed more uniformly than typically anticipated from a stochastic etching. This unique arrangement likely originated from the cooperative linear clustering of epoxy/ether groups evolved from the chemisorption of O_3 on graphene (*33*, *34*). The linear clustering is driven by the low-energy configuration of epoxy/ether groups (*35*, *36*) and is facilitated by a low barrier of diffusion (0.73 to 0.76 eV) of the epoxy groups (*36*, *37*). We measured the apparent energy barrier for the chemisorption of O_3 by counting the coverage of functional oxygen groups using x-ray photoelectron spectroscopy (XPS; fig. S5). An Arrhenius-like plot of the function oxygen coverage rate as a function of the chemisorption temperature yielded an apparent energy barrier of 0.67 eV (Fig. 1F). Accounting for the negative heat of adsorption (physisorption) of O_3 (~0.25 eV) (*38*) in the apparent energy barrier, the energy barrier for chemisorption exceeds the energy barrier of diffusion, which explains the rapid (within milliseconds) formation of the functional oxygen clusters at 250°C.

To investigate the functional oxygen cluster, freshly cleaved highly oriented pyrolytic graphite (HOPG) substrates were gasified in MGR. Because of the smooth surface of HOPG, additional heating after MGR treatment was not needed, and MGR-treated samples were immediately placed in the ultrahigh vacuum (UHV) chamber for the STM imaging. Scanning an area of 30 nm by 30 nm, we could indeed observe several elongated clusters (>10), each surrounding nanometer-sized vacancy defects (Fig. 1G and fig. S6). The clusters seemed to be aligned and had a density of 2.9×10^{12} cm^{-2}, consistent with the observation of vacancy defects on graphene (Fig. 1, D and E). The size of elongated clusters surrounding the vacancy defect was ~2.0 nm by 2.5 nm (Fig. 1H). The height of the cluster was ~2.5 ± 0.2 Å (Fig. 1I), which corresponds to the typical height of the ether group on the graphitic lattice (*35*). A proof of the existence of the clusters also comes from high-temperature annealing experiments where the specimen was heated to 800°C for 2 hours, and as a result, the majority of the functional oxygen cluster was removed as indicated by (i) the smaller size of the features surrounding the vacancy defects (Fig. 1, J and K) and (ii) the maximum height of ~0.6 Å around the vacancy defect (Fig. 1L). We note that the density of vacancy defects did not change upon heating, indicating that only the functional oxygen clusters were removed.

Density functional theory calculations have shown that the ether chains on the graphitic lattice can lead to strain buildup, which eventually unzips the chain. This and the fact that we observe coexistence of clusters with the vacancy defects indicate that the formation of clusters is indeed an intermediary step in the nucleation of vacancy defects in O_3-led gasification of graphene.

Aberration-corrected high-resolution transmission electron microscopy (AC-HRTEM) of N-SLG was carried out to understand the PSD and the diversity of nanopore lattice structure prepared using the same gasification condition as that for STM. To prevent crack formation during the transfer of N-SLG to the microscope grid, a porous polybenzimidazole (PBI) film was deposited on top of N-SLG as a mechanical reinforcement (*39*). The grid was annealed at 900°C in a reducing atmosphere to remove contaminants that mask the SLG lattice (fig. S7). Control experiments on as-synthesized SLG proved that grid preparation steps did not lead to the incorporation of new nanopores (fig. S8), although the loss of the pore-edge functional group could not be avoided. Imaging was carried out using a stable 80-keV beam that did not nucleate or expand nanopores at a small electron dose (figs. S9 and 10 and movies S1 and S2). Overall, a pore density of 1.6×10^{12} cm^{-2}, consistent with the STM findings, was observed. About 49 distinct nanopore lattice structures, missing 1 to 20 carbon atoms, were identified, of which 38 are reported in Fig. 2 (A and B) (fig. S11 and note S3). Among these, the pores where the degree of uncertainty in their structure is high, attributing to edge reconstruction and image resolution, are highlighted in fig. S11. Nonetheless, on the basis of the pore area, the predictability on the number of the missing carbon atom is high in the entire dataset. Several nanopore isomers, defined as pores of different structures formed by removing exactly V number of atoms, were observed. These isomers are referred to as P-V_j. For example, P-10_i, P-10_{ii}, and P-10_{iii} are made by removing 10 carbon atoms but host different structures (Fig. 2, A and B). The relative population of isomers was consistent with the theoretical solution to the isomer cataloging problem of the vacancy defects in graphene (*40*). For example, P-11_i and P-7_i, predicted to be the most probable isomers of P-11 and P-7, respectively, were observed most frequently. No other isomer of P-7_i were observed, perhaps attributing to the extremely high probability of P-7_i (42%) and low probability of other P-7 isomers (<10%). Several high-probability isomers such as P-6_{iii}, P-8_{ii}, P-11_i, P-12_i, P-16_i, and P-17_i were observed filling the gap between the observed and simulation-predicted gas-sieving nanopores (Fig. 2, A and B, and fig. S11) (*40*). Nanopores such as P-10_i, P-13_i, and P-16_i, which have drawn vast attention for gas-sieving, were also observed, albeit they constitute only a small fraction of the nanopore population. PSD based on the number of missing carbon atoms had a majority of nanopores smaller than P-16 (Fig. 2C, top). We also observed a few large elongated nanopores that are likely generated by the coalescence of close-by nanopores during the sample preparation of the microscope grid (fig. S12) and, therefore, are not considered in the statistical analysis. This PSD is highly attractive because pores smaller than P-16 have been predicted to be highly promising for gas separation (*10*, *13*–*16*, *18*). We note that these pores appear unfunctionalized in the AC-HRTEM study because of the tricky TEM

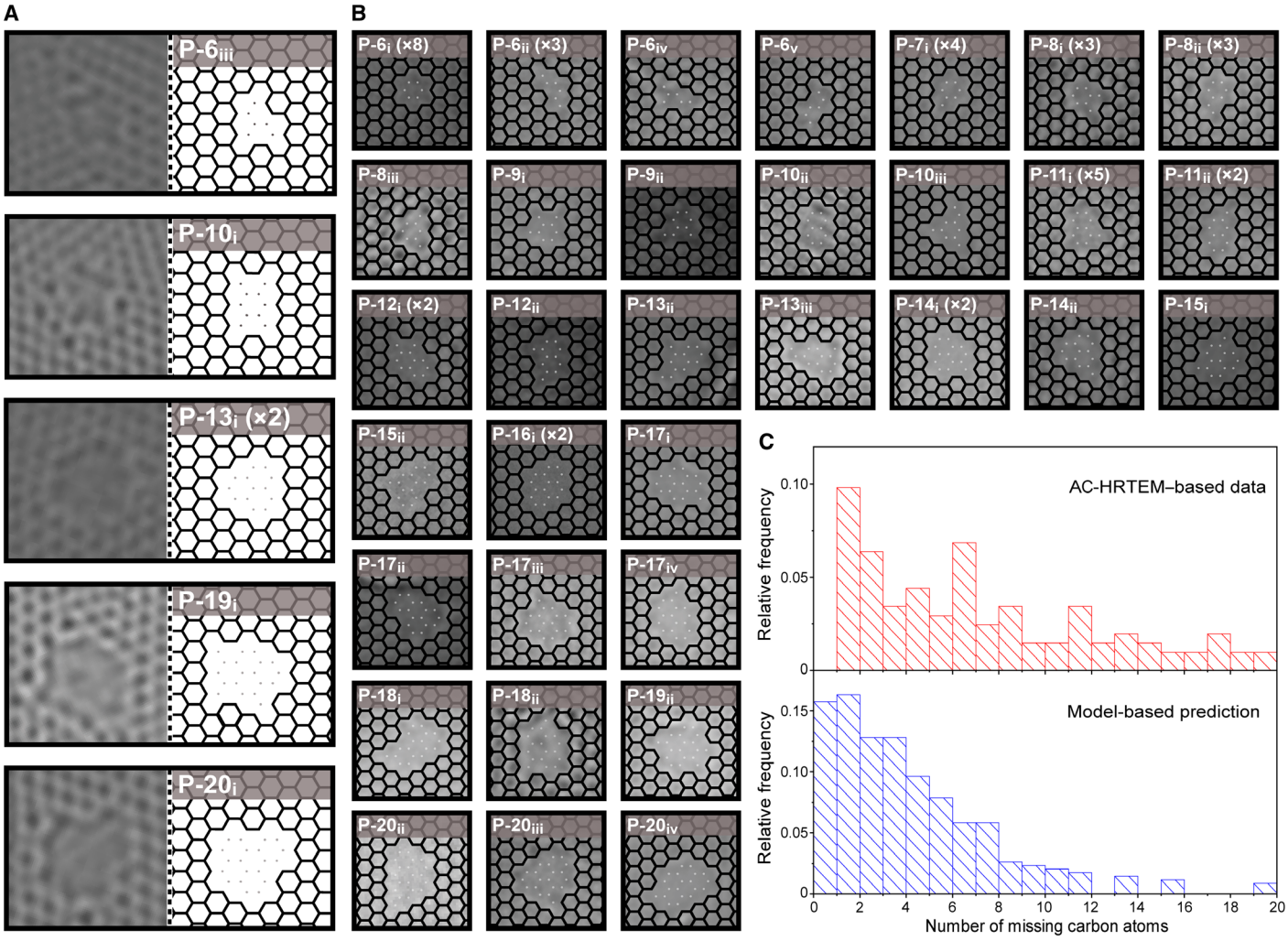

Fig. 2. AC-HRTEM–based analysis of the lattice structure of the vacancy defects incorporated in N-SLG from millisecond gasification. (**A** and **B**) AC-HRTEM images of the vacancy defects and corresponding lattice-fitted structures (dots indicate missing carbon atoms). The repeated occurrence of each defect within the set of images is indicated inside the bracket. For example, P-13i (×2) indicates that P-13i was observed two times. (**C**) Top: Distribution of the number of missing carbon atoms in the vacancy defects based on the AC-HRTEM. Bottom: The predicted distribution of the missing carbon atoms using the gasification kinetics model.

grid cleaning steps, which involved heating the grids at 900°C to desorb contaminants from nanopores for imaging their structure (*39*). This process also removes the edge functional groups that are likely carbonyl groups, as discussed with the STM (Fig. 1, K and L) and XPS data (fig. S13). The presence of these groups will further reduce the electron density gap in the pores from the contribution of carbonyl functional group at the edge and is expected to enhance the molecular selectivity.

Modeling of etching kinetics

The nucleation and growth rates of the vacancy defects in graphene are expected to vary as per the temperature-dependent kinetics of lattice gasification. Etching experiments carried out at 150°C with the same O_3 dose as above yielded much lower pore density than that at 250°C (fig. S14), consistent with the thermally activated chemisorption and clustering of the epoxy groups (*26*, *33*, *37*). To understand the evolution of nanopores and resulting PSD, we modeled the pore nucleation and expansion process. The nucleation density is expected to be proportional to the density of the clusters, which eventually yield a vacancy defect (note S4) and can be expressed as

$$\theta_v = k_c H \int_{t_0}^{t_n} P dt \quad (1)$$

where θ_v is the fractional occupancy of the vacancy defects, P is O_3 pressure, H is Henry's coefficient for physisorption of O_3 on graphene, and k_c is the effective rate constant for the formation of clusters.

To model PSD, we tracked the expansion of pores nucleated during a certain time interval as a function of time (note S4). Briefly, the O_3 exposure was divided into n equal time intervals, Δt. At the end of the O_3 exposure, the number of the missing carbon atoms, v_i, for those pores that nucleated during the time step t_i could be calculated as follows

$$v_i = \sum_{m=i}^{m=n} \frac{\Delta C_m}{\sum_{k=1}^{m} N_k} = \frac{\Delta C_i}{N_1 + N_2 + \ldots N_i} + \ldots\ldots + \frac{\Delta C_n}{N_1 + N_2 + \ldots\ldots + N_n} \quad (2)$$

where N_i is the number of new nuclei generated during a time step i and ΔC_i is the total number of carbon atoms etched from the existing defects in time step i. The PSD extracted by the model is in good agreement with that from the AC-HRTEM observations (Fig. 2C).

CO_2 sieving from graphene nanopores

Membranes were prepared by transferring graphene onto a macroporous W foil, hosting an array of 5-μm pores prepared by laser drilling, using the nanoporous carbon (NPC) film–assisted transfer method (*29*). The 100-nm-thick NPC film is used as a mechanical reinforcement to graphene to assist its crack-free transfer to a macroporous metal support. The pores in NPC film are 20 to 30 nm in size, and therefore, the graphene/NPC interface consists of graphene film resting on NPC pores (fig. S15, A to C). Attributing to the large size of the pores, the NPC film does not sieve gases but transports gases on the basis of the principles of the Knudsen transport where the gas flux is inversely proportional to the square root of its molecular mass. Control experiments based on standalone NPC film yielded large H_2 and CO_2 permeances of 5.6×10^6 and 1.3×10^6 GPU, respectively, with H_2/CO_2, H_2/N_2, H_2/CH_4 selectivities of 4.3, 3.2, and 2.4, respectively (fig. S15, D and E), indicating that NPC film does not sieve gases and only acts as a mechanically reinforcing layer.

Observation of gas flux through NPC-reinforced 1-mm^2-sized N-SLG membranes, prepared using O_3 dosage of 4.8×10^{16} to 3.5×10^{17} molecules cm^{-3} s (τ = 0.01 to 0.2 s), revealed that N-SLG could separate H_2 and CO_2 from CH_4, with H_2 and CO_2 permeances increasing monotonically by 30-fold at the highest O_3 dose (Fig. 3A, figs. S16 and S17, and table S3). The H_2/CH_4 and CO_2/CH_4 selectivities (9.7 to 19.9 and 6.1 to 18.4, respectively) were much higher than the corresponding Knudsen selectivities (2.8 and 0.6, respectively), confirming that the incorporated vacancy defects could sieve similarly sized molecules. The activation energy for H_2, CO_2, and CH_4, extracted by subtracting their heat of adsorption (2.7, 9.9, and 8.3 kJ mol^{-1}, respectively; note S5) from the observed apparent activation energy, did not change significantly (Fig. 3B). The decrease in selectivity at higher dosage can be attributed to the coalescence of adjacent pores, which is expected to promote the effusive transport (*19*).

Hindering the etching reaction with the synchronized Ar purge (t_d = 0–1.0 s) improved the CO_2 sieving performance (Fig. 3C and table S4). CO_2 permeance of 2620 GPU with corresponding CO_2/N_2 and CO_2/CH_4 selectivities of 27.6 and 20.0 could be achieved at O_3 dose of 1.6×10^{17} molecules cm^{-3} s (τ = 0.1 s, t_d = 0.5 s). The rapid removal of residual O_3 by the Ar purge was also reflected in the fact that a relatively lower structural disorder was observed by the Raman spectroscopy (fig. S3C). The use of purge improved CO_2/CH_4 selectivity without a significant loss in CO_2 permeance (Fig. 3C). We noted that the sieving of CO_2 from N_2 corresponded to a resolution of 0.3 Å in molecular differentiation. We could also achieve CO_2/O_2 selectivity of 12.6, corresponding to a resolution of 0.2 Å.

The controlled etching kinetics yield attractive CO_2/CH_4 selectivities at a wide range of temperatures (120° to 290°C) with optimized O_3 dosages (Fig. 3D and figs. S18 to S20). For a given ozone dose (τ = 0.1 s, t_d = 0.5 s), we observed increasing gas permeance and decreasing selectivity as a function of the etching temperature, attributing to the faster etching kinetics at the higher temperature. For example, HRTEM-based study of the distribution of edge-to-edge van der Waals gap (*18*) indicated that etching at 290°C increased the mean gap by ~0.2 nm from that obtained at 250°C (Fig. 3E). As mentioned before, these pores are unfunctionalized in the HRTEM study because of the TEM grid preparation steps. The actual distribution of van der Waals gap is expected to be shifted to the left (by ~2.4 Å) from the contribution of carbonyl functional group at the pore edge. We show that the mean gap could be reduced by optimizing the O_3 dose, i.e., by reducing t_d from 0.5 to 0.2 s and using a cooled He purge. This was reflected in the improvements in the H_2/N_2 and CO_2/N_2 selectivities (Fig. 3D).

The controlled gasification of graphene by millisecond etching is highly scalable, attributing to the highly uniform etching of graphene under the partial vacuum in MGR (fig. S3B). To demonstrate this, we gasified an SLG sized 2 cm by 1.5 cm and subsequently transferred it to a smoothened metal-mesh support. Attributing to the higher roughness of the metal-mesh compared to the drilled W foil, the transfer became more challenging, and therefore, the mechanical reinforcement was switched from the NPC film to a nanoporous polymer film, poly[1-(trimethylsilyl)-1-propyne] (PTMSP) (*23*, *24*). Briefly, the mechanically reinforcing PTMSP layer was coated on N-SLG before its transfer to the porous support. The resulting centimeter-scale PTMSP-reinforced N-SLG membrane (Fig. 3F) yielded a CO_2/N_2 separation factor of 17.3 at 25°C (table S6). In contrast, the selectivity of the standalone PTMSP film, prepared by the same method (coating on Cu foil followed by transfer to the support by etching the foil), was ~10 (*23*, *24*). The value is similar to that from millimeter-scale PTMSP-reinforced N-SLG membrane (22.5) and that from the NPC-reinforced N-SLG membranes prepared on the drilled W support, confirming that the gasification technique reported here is scalable.

Adjustment of the molecular cutoff

Molecular sieving from N-SLG has a unique advantage that one can adjust the molecular cutoff for a specific separation application. We demonstrate this by expanding vacancy defects using O_2 at 200°C in situ in the membrane module. Briefly, the feed side of N-SLG membrane pre-etched in MGR was pressurized with CO_2/N_2 mixture, while the permeate side was swept with Ar, and a steady-state operation was achieved. To initiate the etching, the sweep gas was switched to O_2. Subsequently, the partial pressure of CO_2 and N_2 in the permeate side was tracked as a function of time using an online mass spectrometer (MS). After the reaction, the sweep was switched back to Ar to measure the gas permeance.

Upon O_2 exposure at 200°C, CO_2 and N_2 concentrations in the permeate side increased as a function of time (Fig. 4A). However, the increase in the CO_2 concentration was much more rapid, which resulted in the improvement of CO_2 permeance and CO_2/N_2 selectivity (Fig. 4, B and C, and fig. S23). The improvement in the performance was permanent and could be observed after several cycles of testing over several days. Repeating O_2-based pore expansion, on the same N-SLG after several days, led to further improvement in permeance, while the selectivity did not change considerably (Fig. 4, A to C, and tables S7 and S8). In contrast, the treatment of membranes with O_3 at 25°C, which does not lead to lattice etching but pore edge functionalization (*29*), led to a decrease in the gas permeance (green trace in Fig. 4B), further confirming that O_2 treatment at 200°C leads to pore expansion.

The slow pore expansion with O_2 could shift the molecular cutoff by 0.1 Å, consistent with the etching kinetics of graphite with O_2 at 200°C. Assuming first-order etching kinetics with O_2, we estimate an etching rate constant of 1.6×10^{-7} nm min^{-1} $torr^{-1}$ at these conditions (note S6) (*26*, *41*, *42*). As a result, the pore expansion for 1 to

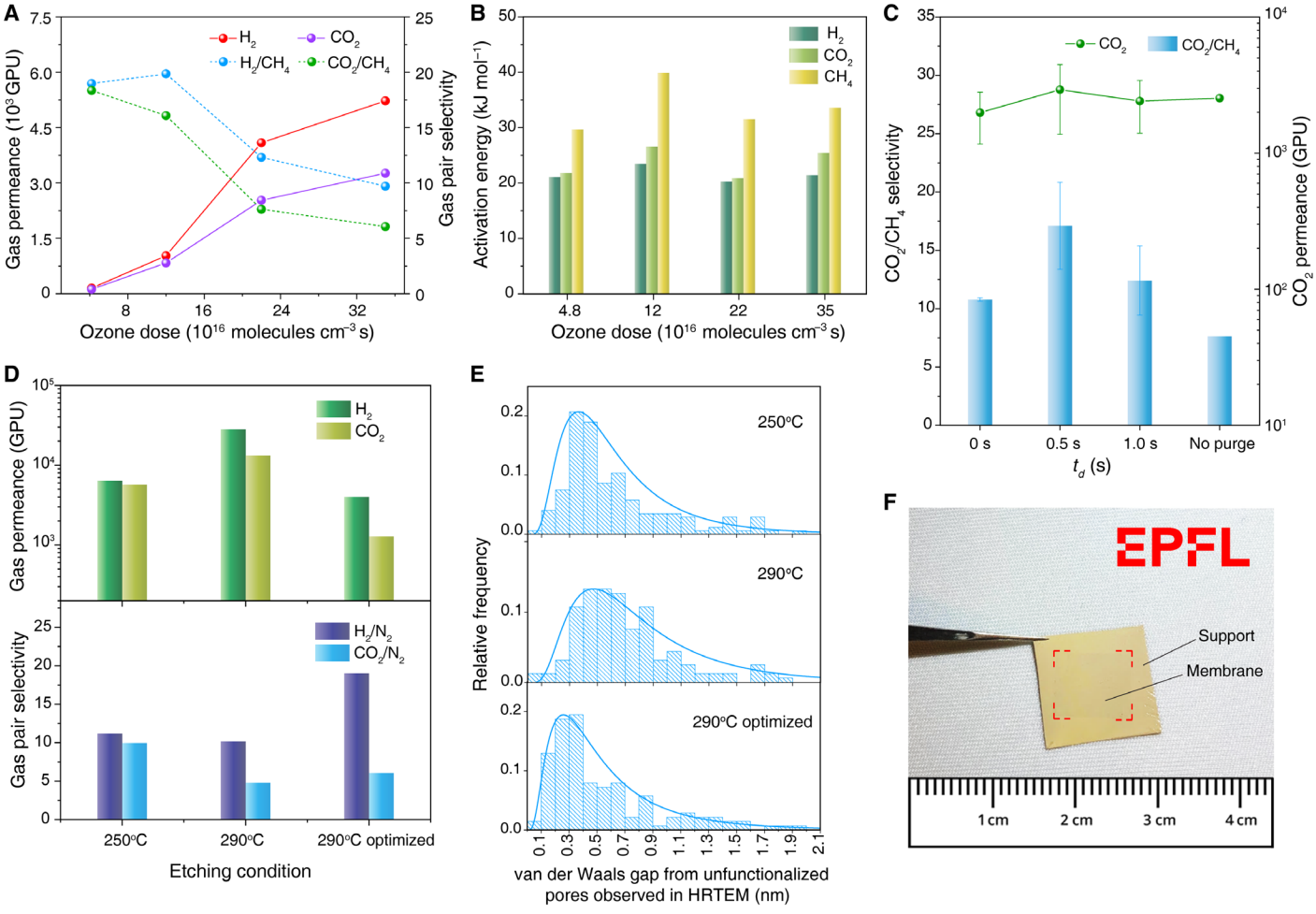

Fig. 3. Gas separation performance from the vacancy defects in N-SLG incorporated by the millisecond gasification. Evolution of the gas permeance (**A**) and extracted activation energies of H_2, CO_2, and CH_4 for transport across N-SLG (**B**) as a function of the O_3 dosage. (**C**) CO_2/CH_4 selectivity and CO_2 permeance from N-SLG etched at 250°C ($\tau = 0.1$ s) with varying t_d. (**D**) Comparison of the gas separation performance of N-SLG etched at 250° and 290°C and (**E**) the corresponding van der Waals gap extracted from HRTEM after heating the samples to 900°C (unfunctionalized pores). t_d was 0.5 s for the 250° and 290°C cases (using Ar purge) and 0.2 s for the optimized 290°C case (using the He purge). (**F**) Photograph of the centimeter-scale N-SLG membrane on the smoothened metal-mesh support. Red lines highlight the edges of the membrane. Photo credit: Shiqi Huang, École Polytechnique Fédérale de Lausanne.

2 hours favored O_2 permeation, reducing CO_2/O_2 selectivity from 12.6 to 7.4 and increasing O_2/N_2 selectivity from 1.6 to 3.4 (Fig. 4C). Combined with O_2 permeance of 1300 GPU, it makes N-SLG membranes attractive for the decentralized O_2/N_2 separation for enriching O_2 (*43*). In the context of postcombustion capture, the shifted cutoff allowed us to realize extremely attractive CO_2/N_2 separation performance with CO_2 permeance and CO_2/N_2 selectivity of 9600 GPU and 24.4, respectively (Fig. 4D and table S9). Another membrane yielded CO_2 permeance of 11,850 GPU and CO_2/N_2 selectivity of 21.7. The CO_2/N_2 separation performance from a mixed feed (20% CO_2) was similar to that from the single component with the mixture separation factors approximately 10% higher than the corresponding ideal selectivities (fig. S24), which can be attributed to competitive adsorption of CO_2 over N_2. We did not observe irreversible pore shrinkage or physical aging during the elevated temperature (120°C) stability testing (*44*), and the performance was stable for a period of 3 weeks (fig. S25). We performed a techno-economic analysis (note S7) of a high-scale membrane process for postcombustion CO_2 capture based on the obtained N-SLG membranes. The optimal configuration to achieve recovery and purity equal to 90% was a double stage with recycle of the second retentate and vacuum in the permeate channels (fig. S26). The lowest energy consumption (1.3 MJ/kg_{CO2}) was found with the N-SLG membrane yielding CO_2 permeance and CO_2/N_2 selectivity of 9600 GPU and 24.4, respectively, using inlet CO_2 concentration of 13.5% and optimized permeate pressures of 0.04 and 0.1 bar in the two stages. The corresponding capture penalty, with specific membrane cost of \$500/m^2 and electricity cost of \$0.04 per kilowatt-hour, was equal to \$31.5/ton_{CO2}. This capture penalty makes the N-SLG membrane–based process very competitive with the state-of-art absorption (capture penalty of around \$50/ton_{CO2}) (*7*) and with the polymeric membrane–based capture processes (capture penalty between \$25/ton_{CO2} and \$40/ton_{CO2}) (*6*).

DISCUSSION

Overall, we report a scalable lattice gasification technique bringing two critical components of the lattice etching kinetics: (i) the use of

high temperature to promote rapid chemisorption of O_3 on graphene, leading to a functional oxygen clusters, which eventually nucleate the high-density vacancy defects (>10^{12} cm^{-2}) for gas separation, similar to those reported for liquid separation (*45*, *46*), and (ii) millisecond reaction time that limits the expansion of vacancy defects to yield CO_2-sieving nanopores with a resolution of 0.2 to 0.3 Å in molecular differentiation. The in situ pore expansion experiments demonstrate that the graphene nanopore presents a unique opportunity to shift the molecular cutoff by a fraction of angstrom. Both gasification and pore expansion techniques are highly predictable and reproducible, which will pave the way to fabricate nanopores in SLG for separating several species based on the relative differences in size, even if the size difference is much smaller than 1 Å, including isotope purification (*47*), ion-ion separation (*48*), and organic solvent nanofiltration (*49*). The method demonstrated here takes one step closer to achieve the target of incorporating vacancy defects in graphene with the precision of a few atoms, a major goal of material science and chemistry.

MATERIALS AND METHODS

Annealing of commercial Cu foil

The commercial Cu foil (Alfa Aesar, 99.8% purity and 25 μm, or Strem Chemicals Inc., 99.9% purity and 50 μm) was thermally annealed in a furnace equipped with a high-purity alumina tube (99.8% purity). The high-purity alumina tube reduced the silica contaminations on the Cu foil. The annealing was done in three steps. First, the Cu foil was placed inside the furnace and heated to 1000°C in a CO_2 atmosphere at 700 torr to remove the organic contamination (*50*). Second, CO_2 was purged out and a H_2/Ar mixture (10:90 ratio) was filled to a pressure of 700 torr. Third, the temperature of the furnace was increased to 1075°C and was maintained at this temperature for 1 hour. Subsequently, the furnace was cooled down to 1000°C at a rate of 0.1°C min^{-1} and then to room temperature by natural convection.

Graphene growth on Cu foil

SLG was synthesized in an LPCVD setup on the surface of the annealed Cu foil (*27*, *51*). Briefly, the foil was heated to 1000°C in a CO_2 atmosphere at 700 torr and kept there for 30 min to remove the organic contaminations. Then, the CO_2 flow was stopped, and the chamber was evacuated. Following this, a flow of 8 standard cubic centimeters per minute (sccm) of H_2 was introduced for 30 min. Then, a flow of 24 sccm of CH_4 was added, maintaining a total pressure of 460 mtorr for 30 min, leading to the growth of polycrystalline SLG film. Last, the growth chamber was cooled rapidly to room temperature while maintaining the H_2 flow.

Etching of graphene in MGR

The as-synthesized SLG supported on the Cu foil was etched in the homemade MGR setup (Fig. 1A and fig. S2A). The MGR consisted of a 10-cm-long temperature-controlled reaction zone with three inlets and an outlet. One inlet was connected to a reservoir storing pressurized O_3/O_2 mixture. The reservoir, in turn, was connected to an O_3 generator (Atlas 30, Absolute Ozone) supplying 9 mole percent O_3 in O_2. The second inlet of MGR was connected to purge gas supply (Ar or liquid nitrogen–cooled He). Two MLVs (atomic layer deposition valve, Swagelok) controlled a synchronized injection of O_3 and the purge gas to the MGR. The O_3 dose was controlled by opening the MLV for a short time and purging the MGR after a short delay (table S2 and notes S1 and S2). The third inlet of MGR was connected to H_2/Ar supply. The role of this supply was to maintain a reducing atmosphere in the reactor before and after the gasification. The outlet of MGR was connected to a vacuum pump via an outlet valve. The MGR was heated using a heating tape wrapped around the reaction zone, and the heating was controlled using a feedback controller using input from a thermocouple placed inside the gasification zone.

For the etching of SLG, the following procedure was used. As-synthesized SLG was heated inside the reaction zone of MGR in a H_2 atmosphere. Before etching, H_2 was purged out with Ar while maintaining a chamber pressure of 0.8 torr. A custom LabVIEW program was used to open the O_3 MLV for a short time (0.01 to 0.2 s) and, optionally, to open the purge valve after a certain delay (0 to 1 s). After etching, the sample was cooled down to room temperature in an Ar atmosphere. We noticed oxidation of Cu during etching, and therefore, for further use, the sample was annealed at 300°C in a H_2 atmosphere to reduce the oxidized Cu.

Fabrication of membrane

The fabrication of the 1-mm^2-sized graphene membrane on a macroporous tungsten support was similar to the previously reported method (*29*). Briefly, an NPC film was deposited on N-SLG as a mechanically reinforcing layer. The NPC/N-SLG/Cu was floated on a $Na_2S_2O_8$ solution [20 weight % (wt %) in water] to etch the Cu foil. After Cu etching, the floating NPC/N-SLG film was rinsed in deionized water to remove the residues. Last, the floating NPC/N-SLG film was scooped on the macroporous W support hosting laser-drilled 5-μm pores to fabricate N-SLG membrane.

The N-SLG membrane prepared using PTMSP reinforcement was fabricated in quite a similar way as above. First, a 1.25 wt % of PTMSP solution in toluene was used to spin coat a PTMSP layer on N-SLG surface (around 0.5 ml of PTMSP solution for 1-cm^2 coating area). The spin-coating speeds used to prepare the thin film are as follows: 1000 rpm for 30 s and then 2000 rpm for 30 s. Next, the PTMSP/N-SLG/Cu was inserted in a vacuum oven at 25°C for 12 hours to completely remove the solvent from PTMSP. Subsequently, the PTMSP/N-SLG/Cu was floated on a 1 M $FeCl_3$ solution to etch the Cu foil. Last, the floating PTMSP/ N-SLG film was scooped on the macroporous W support to fabricate 1-mm^2-sized graphene membrane or smoothened macroporous metal-mesh support to fabricate the centimeter-scale N-SLG membrane.

Gas permeation test

The single-component and mixture gas permeation tests were carried out in a homemade permeation module. All the permeation tests were conducted in the open-end mode. All equipment used in the permeation setup [the mass flow controllers (MFCs), oven, and MS] were calibrated within a 5% error. The N-SLG membranes on tungsten supports were directly sandwiched in the VCR-based module (Swagelok VCR fittings), making a leak-tight metal-to-metal seal. The centimeter-scale N-SLG membranes were fixed to an annular stainless steel disk using epoxy and then sandwiched using viton o-rings to ensure a gas-tight seal between the annular disk and the membrane module. The feed and the sweep lines were preheated inside the oven to prevent temperature fluctuation. An MFC regulated the flow rate of the feed gas, where the feed pressure (1.5 to 2.0 bar) was adjusted by the back-pressure regulator. Another MFC controlled the flow rate of sweep gas (Ar) with 1-bar pressure. The sweep gas

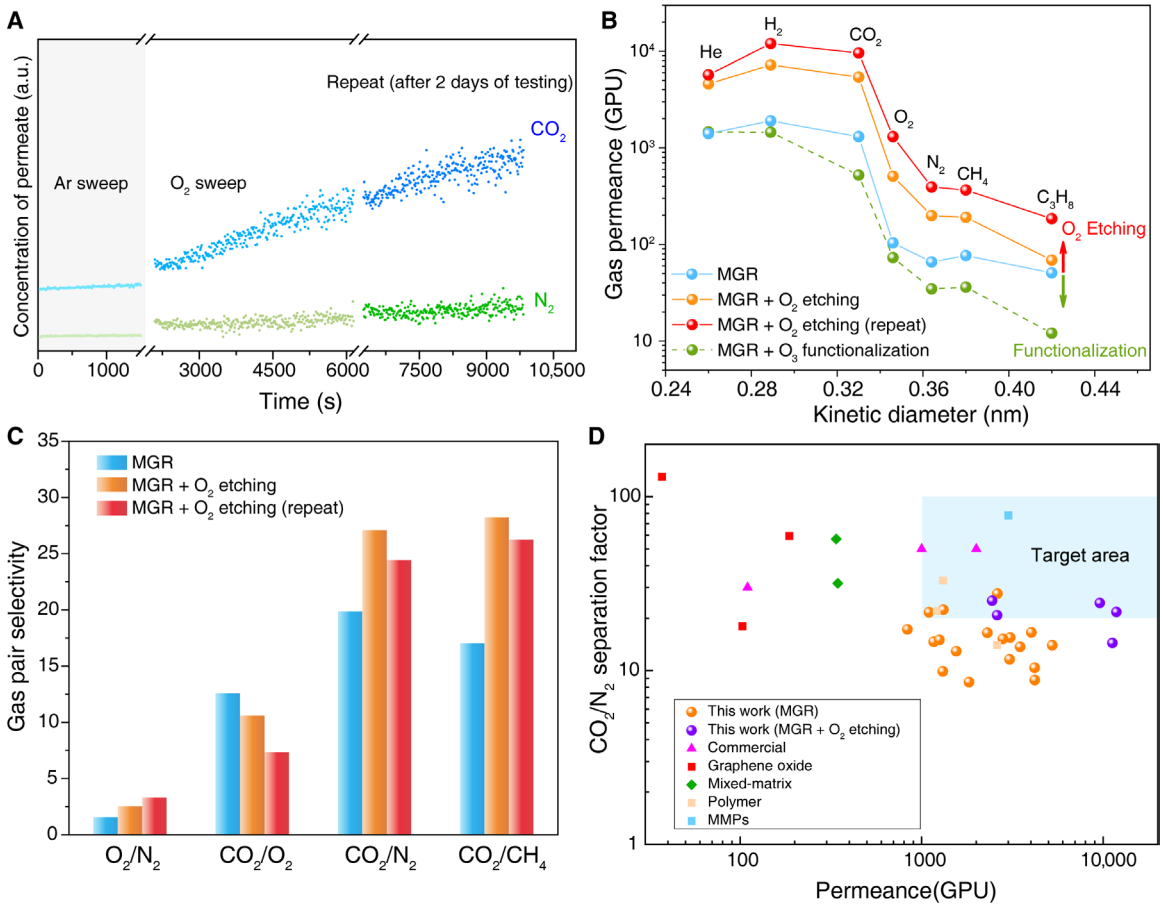

Fig. 4. Gas separation performance of N-SLG prepared by MGR followed by in situ O_2 treatment at 200°C. (**A**) CO_2 and N_2 evolution in the permeate side during the in situ etching. (**B**) Gas permeance at 25°C as a function of the kinetic diameter from the as-prepared N-SLG membrane, from those subjected to the in situ O_2 treatment, and from that subjected to O_3 at 25°C for 2 min. The term "repeat" refers to repeating the in situ O_2 treatment after 2 days of gas permeance testing. (**C**) Comparison of the gas pair selectivity data at 25°C of the as-prepared N-SLG membrane with those subjected to the in situ O_2 treatment. (**D**) Comparison of the CO_2/N_2 mixture separation performance from the membranes prepared in this study with the state-of-the-art membranes for postcombustion capture. The target area refers to the membrane performance needed to surpass the energy efficiency of the amine-based absorption process (*6*, *7*). MMPs, metal-induced ordered microporous polymers.

carried the permeate gas to the MS for real-time analysis of the permeate concentration. The MS was calibrated for the concentration range measured in the permeate stream for He, H_2, CO_2, O_2, N_2, CH_4, and C_3H_8 in Ar. Before testing, all membranes were heated to 100°C to remove the atmospheric contaminations on the graphene surface. For the mixture permeation tests, an equimolar gas mixture (or a 20:80 mixture of CO_2/N_2 whenever specified) was used on the feed side. The performance of the membranes was tracked continuously in real time. The gas flux was calculated once the steady state was established. Only the steady-state permeation data are reported.

In situ oxygen etching

O_2 etching was conducted on the suspended N-SLG membrane inside the membrane module. A metal-metal (Swagelok VCR fittings) seal, where the membrane was sandwiched in the VCR-based module, was used to ensure a leak-proof system. Before the oxygen etching, the membrane module with the membrane inside was heated to 100°C to remove the adsorbed atmospheric contaminations and the gas separation performance was measured. Following this, the membrane was heated to 200°C using Ar as the sweep and a CO_2/N_2 mixture in the feed side. The online MS monitored the CO_2 and N_2 concentration in the permeate side continuously. To start the in situ etching, the Ar flow in the sweep (permeate side of the membrane) was swapped with an O_2 flow. The permeate concentration was monitored as a function of time to evaluate the effect of the etching on the gas-sieving property of the membrane. After the etching reaction, the sweep was swapped back to Ar and the steady-state membrane performance was measured.

Raman characterization

Raman characterization was carried on graphene transferred onto the SiO_2/Si wafer by the wet-transfer method. The N-SLG/Cu was spin-coated with a thin poly(methyl methacrylate) (PMMA) layer (950 PMMA A4, 4% in anisole; MicroChem Corp.). After the coating, the PMMA/N-SLG/Cu was annealed at 60°C for 30 min to remove the solvent. Then, the PMMA/N-SLG/Cu was floated on a 20% $Na_2S_2O_8$ solution to remove the Cu foil. Following this, the floating film was transferred to deionized water to rinse the residual etchant and was scooped by SiO_2/Si wafer. To increase the bonding of PMMA/N-SLG, the sample was annealed at 150°C and then 190°C for 10 min. Last, PMMA was removed by acetone leaving N-SLG on the SiO_2/Si wafer for Raman characterization.

Single-point data collection and mapping were performed using Renishaw micro-Raman spectroscope equipped with a blue laser (λ_L = 457 nm, E_L = 2.71 eV) and a green laser (λ_L = 532 nm, E_L = 2.33 eV). Analysis of the Raman data was carried out using MATLAB. For calculation of the D and the G peak height, the background was subtracted from the Raman data using the least-squares curve fitting tool (lsqnonlin).

Sample preparation for TEM

The transfer-induced contaminations on the N-SLG surface were minimized by fabricating a thin PBI film and then transferring graphene on a TEM grid with the help of this film (fig. S7). The porous PBI was prepared separately and adhered on top of graphene, which allowed us to avoid polymer solution–induced contaminations on the surface of N-SLG. These contaminations are difficult to avoid when directly forming the porous film on top of graphene (*19*, *24*) or when using a PMMA-based transfer approach (*52*). The N-SLG domain resting in the micrometer-sized open areas of the porous PBI film was easy to find in the imaging conditions of AC-HRTEM (fig. S7). The porous PBI reinforcement layer was made of a thermally resistant PBI (fumion AM provided by FUMATECH BWT GmbH, Germany), which can be carbonized once it sits on top of N-SLG to form a thermally conductive carbon porous reinforcement ideal for AC-HRTEM imaging.

A thin porous PBI film was prepared using the nonsolvent induced phase separation (NIPS) process. Briefly, a drop of a 1.5 wt % solution of PBI in dimethylacetamide was spread on top of a 25-μm-thick Cu foil by gently pressing it with a glass slide. The wet coating was immersed in an isopropanol bath to initiate phase separation, which led to a thin porous polymer film. After drying the resulting film, the Cu foil was etched and the floating porous PBI film was transferred to a water bath to rinse the residues from the etching step. Last, the floating film was scooped out of the water bath using as-prepared N-SLG on Cu foil. After drying the porous PBI film, a drop of isopropanol was poured on it, which enhanced the adhesion of the film to the N-SLG surface upon the evaporation of isopropanol. Subsequently, the porous PBI film resting on N-SLG/Cu was pyrolyzed at 500°C in the flow of H_2/Ar, leading to the formation of porous carbon. Next, the Cu foil was etched, and the resulting reinforced N-SLG was washed with water and transferred to a 400-mesh gold TEM grid (fig. S7A).

Before AC-HRTEM, the TEM grid was cleaned inside activated carbon in a H_2 atmosphere at 900°C for 1 hour to remove the contaminations covering the nanopores. The cleaning was carried out in a temperature- and environment-controlled furnace, taking the following precautions to avoid the presence of O_2 in the system, which could enlarge the pores: (i) The adsorbed gases on the N-SLG surface were removed by evacuating the system at 2 mtorr at 200°C for 2 hours; (ii) a positive pressure was maintained in the furnace (850 torr of H_2) while heating the sample to 900°C to avoid O_2 leak in the system. A control sample consisting of as-synthesized SLG (without the gasification step) was loaded in the furnace together with the N-SLG sample. The analysis of the control sample confirmed that the sample preparation did not nucleate vacancy defects in the graphene lattice (fig. S8).

HRTEM imaging

HRTEM imaging was performed using a Talos F200X (FEI) microscope operated at an acceleration voltage of 80 kV. The dose rate was maintained at ~500 $e^- s^{-1} Å^{-2}$ during imaging. To reveal the nanopores and to verify that the pores did not expand during imaging, the following procedure was followed: (i) Thirty consecutive images were taken with an exposure time of 2 s each. (ii) The first and last images were compared to verify that no pore expansion occurred during imaging. (iii) The first five to eight images were integrated to form the final image. Typically, during HRTEM imaging of the nanoporous graphene samples in Talos, the pores experienced a dose of ~8×10^3 $e^- Å^{-2}$ during focusing and imaging.

AC-HRTEM imaging

AC-HRTEM was performed using a double-corrected Titan Themis 60-300 (FEI) equipped with a Wein-type monochromator. An 80-keV incident electron beam was used for all experiments to reduce the electron radiation damage. The incident electron beam was monochromated ("rainbow" mode illumination) to reduce the effects of chromatic aberration, and a negative Cs of ~17 to 21 μm with a slight overfocus was used to give a "bright atom" contrast in the images. The dose rate was maintained at ~2×10^4 $e^- s^{-1} Å^{-2}$ during imaging, and a slit was used to expose only the area of the sample being imaged to the electron beam.

The maximum energy that can be transferred to a carbon atom by an 80-keV incident electron is 15.8 eV, which is below the knock-on energy threshold for carbon atoms in the basal plane of graphene (*53*). In agreement, we did not observe any knock-on from pristine areas during imaging. Similar to the literature (*53*), we observed reconfiguration of the pore edge in the scale of seconds and, on occasions, in less than a second. The knock-on of edge atoms (i.e., the expansion of vacancy defects) was observed only after a longer exposure time (figs. S9 and S10 and movies S1 and S2). The pores imaged to construct the pore library of the graphene samples prepared by MGR were exposed to doses that were low enough to avoid the expansion. Typically, during imaging of the N-SLG samples, the lattice experienced a dose of ~2×10^5 $e^- Å^{-2}$ during focusing and imaging. The first 5 to 10 frames (each frame corresponds to a dose of ~5×10^3 $e^- Å^{-2}$) were integrated into the final image. When needed, the images were processed with a combination of Gaussian, average, and/or band-pass filters to make the lattice clearer.

Analysis of AC-HRTEM images

The graphene lattice surrounding the vacancy defects was manually fitted with a hexagonal lattice to locate the missing carbon atoms. Dangling bonds and Stone-Wales defects were ignored. This analysis is a powerful tool to quantify the number of missing atoms and to draw the shape of the defects in a large library of structures (49 distinct structures). We note the uncertainty in the edge configuration of the vacancy defect because edge reconfiguration was present at the imaging conditions (80 keV; figs. S9 and S10 and movies S1 and S2). A total of 118 defects from three independently prepared samples were analyzed. The library containing the raw and the fitted images of all the defects is available in fig. S11.

The diameter of the defects was determined using the ImageJ software. The diameter was calculated by fitting the largest possible circle that fitted inside the defect as shown in fig. S22. Only pores surrounded by the graphene lattice were used for the analysis (i.e., pores touching contamination were ignored).

STM imaging

STM imaging was carried by using a low-temperature STM (CreaTec Fischer & Co. GmbH). To remove contamination from the graphene

surface, the N-SLG/Cu samples were annealed/reduced under 50-sccm H_2 flow, at 800 torr and 900°C for 3 hours in a quartz tube furnace. This treatment was necessary for successful STM analysis of Cu foil–supported samples because after the MGR treatment, the Cu surface became oxidized and rough. Immediately after the 900°C annealing, the sample was transferred to the UHV chamber of the STM. The N-SLG samples were again heated inside the UHV chamber at 900°C for 3 hours to clean the surface from residual contamination. STM imaging was performed at 77 K and a pressure of 2×10^{-10} mbar. The MGR-treated HOPG (Mosaic Spread 0.3-0.5 degree, ScanSens) sample was transferred to a UHV chamber immediately after MGR treatment, and STM imaging was performed at 77 and 4.2 K. The STM probe was prepared by cutting a commercial Pt/Ir wire (Pt: 90 wt % and diameter of 0.25 mm; Alfa Aesar). The tilt in the acquired STM images was reduced by flattening in the WSxM software (*54*).

X-ray photoelectron spectroscopy

The XPS measurements on O_3-treated graphene resting on Cu foil were carried out on an Axis Supra (Kratos Analytical) using the monochromated Kα x-ray line of an aluminum anode. The pass energy was set to 20 eV, and the step size was set to 0.1 eV. The samples were grounded; thus, the binding energies are presented without any correction. The XPS spectra were processed with CasaXPS, with background subtraction by the Shirley method.

Other characterizations

Scanning electron microscopy (SEM) imaging was carried out by using a FEI Teneo scanning electron microscope at 1.0 to 2.0 kV and working distances of 4.0 to 9.0 mm. No conductive coating was applied to the substrates before SEM. X-ray diffraction measurements were carried out in a Bruker D8 DISCOVER x-ray diffractometer that was equipped with a laser-based sample alignment system.

Density functional theory calculations for the heat of adsorption

The density functional theory calculations were performed using the Quantum ESPRESSO package (*55*, *56*) to study the potential energy surface of H_2, N_2, CO_2, and CH_4 on the N-SLG lattice hosting two types of vacancy defects (P-13_i and P-16_i). To represent the plane wave charge density, an energy cutoff of 70 rydberg was used. The defects were incorporated in a graphene lattice large enough to mimic an infinite sheet and avoid any interactions among pores. The Brillouin zone was expressed with uniform $3 \times 3 \times 1$ k-point grids. To prevent interactions between the adjacent lattice, a vacuum region of 40 Å was used in the *z* direction. Calculations were performed by ultrasoft pseudopotentials (*57*, *58*); the second version of the van der Waals density functional (vdW-DF2) dispersion correction was used to correct noncovalent forces (*59*).

SUPPLEMENTARY MATERIALS

Supplementary material for this article is available at http://advances.sciencemag.org/cgi/content/full/7/9/eabf0116/DC1

REFERENCES AND NOTES

1. A Research Agenda for Transforming Separation Science (National Academies Press, 2019), doi:10.17226/25421.
2. X. Ma, P. Kumar, N. Mittal, A. Khlyustova, P. Daoutidis, K. A. Mkhoyan, M. Tsapatsis, Zeolitic imidazolate framework membranes made by ligand-induced permselectivation. *Science* **361**, 1008–1011 (2018).
3. S. Zhou, Y. Wei, L. Li, Y. Duan, Q. Hou, L. Zhang, L. X. Ding, J. Xue, H. Wang, J. Caro, Paralyzed membrane: Current-driven synthesis of a metal-organic framework with sharpened propene/propane separation. *Sci. Adv.* **4**, eaau1393 (2018).
4. C. Zhang, W. J. Koros, Ultraselective carbon molecular sieve membranes with tailored synergistic sorption selective properties. *Adv. Mater.* **29**, 1701631 (2017).
5. M. Lozada-Hidalgo, S. Hu, O. Marshall, A. Mishchenko, A. N. Grigorenko, R. A. W. Dryfe, B. Radha, I. V. Grigorieva, A. K. Geim, Sieving hydrogen isotopes through two-dimensional crystals. *Science* **351**, 68–70 (2016).
6. T. C. Merkel, H. Lin, X. Wei, R. Baker, Power plant post-combustion carbon dioxide capture: An opportunity for membranes. *J. Membr. Sci.* **359**, 126–139 (2010).
7. S. Roussanaly, R. Anantharaman, K. Lindqvist, H. Zhai, E. Rubin, Membrane properties required for post-combustion CO_2 capture at coal-fired power plants. *J. Membr. Sci.* **511**, 250–264 (2016).
8. Y. Yamada, K. Murota, R. Fujita, J. Kim, A. Watanabe, M. Nakamura, S. Sato, K. Hata, P. Ercius, J. Ciston, C. Y. Song, K. Kim, W. Regan, W. Gannett, A. Zettl, Subnanometer vacancy defects introduced on graphene by oxygen gas. *J. Am. Chem. Soc.* **136**, 2232–2235 (2014).
9. G.-D. Lee, C. Z. Wang, E. Yoon, N. M. Hwang, D. Y. Kim, K. M. Ho, Diffusion, coalescence, and reconstruction of vacancy defects in graphene layers. *Phys. Rev. Lett.* **95**, 205501 (2005).
10. D. Jiang, V. R. Cooper, S. Dai, Porous graphene as the ultimate membrane for gas separation. *Nano Lett.* **9**, 4019–4024 (2009).
11. K. Celebi, J. Buchheim, R. M. Wyss, A. Droudian, P. Gasser, I. Shorubalko, J.-I. J.-I. Kye, C. Lee, H. G. Park, Ultimate permeation across atomically thin porous graphene. *Science* **344**, 289–292 (2014).
12. H. Li, Z. Song, X. Zhang, Y. Huang, S. Li, Y. Mao, H. J. Ploehn, Y. Bao, M. Yu, Ultrathin, molecular-sieving graphene oxide membranes for selective hydrogen separation. *Science* **342**, 95–98 (2013).
13. C. Sun, M. S. H. Boutilier, H. Au, P. Poesio, B. Bai, R. Karnik, N. G. Hadjiconstantinou, Mechanisms of molecular permeation through nanoporous graphene membranes. *Langmuir* **30**, 675–682 (2014).
14. H. Liu, Z. Chen, S. Dai, D. Jiang, Selectivity trend of gas separation through nanoporous graphene. *J. Solid State Chem.* **224**, 2–6 (2015).
15. Z. Yuan, A. Govind Rajan, R. P. Misra, L. W. Drahushuk, K. V. Agrawal, M. S. Strano, D. Blankschtein, Mechanism and prediction of gas permeation through sub-nanometer graphene pores: Comparison of theory and simulation. *ACS Nano* **11**, 7974–7987 (2017).
16. F. Vallejos-burgos, F.-X. Coudert, K. Kaneko, Air separation with graphene mediated by nanowindow-rim concerted motion. *Nat. Commun.* **9**, 1812 (2018).
17. S. P. Koenig, L. Wang, J. Pellegrino, J. S. Bunch, Selective molecular sieving through porous graphene. *Nat. Nanotechnol.* **7**, 728–732 (2012).
18. L. Wang, M. S. H. Boutilier, P. R. Kidambi, D. Jang, N. G. Hadjiconstantinou, R. Karnik, Fundamental transport mechanisms, fabrication and potential applications of nanoporous atomically thin membranes. *Nat. Nanotechnol.* **12**, 509–522 (2017).
19. J. Zhao, G. He, S. Huang, L. F. Villalobos, M. Dakhchoune, H. Bassas, K. V. Agrawal, Etching gas-sieving nanopores in single-layer graphene with an angstrom precision for high-performance gas mixture separation. *Sci. Adv.* **5**, eaav1851 (2019).
20. P. M. Ajayan, T. W. Ebbesen, J. S. Williams, Reports on progress in physics related content irradiation effects in carbon nanostructures irradiation effects in carbon nanostructures. *Reports Prog. Phys. Irradiat.* **62**, (1999).
21. J. Buchheim, R. M. Wyss, I. Shorubalko, H. G. Park, Understanding the interaction between energetic ions and freestanding graphene towards practical 2D perforation. *Nanoscale* **8**, 8345–8354 (2016).
22. C. J. Russo, J. A. Golovchenko, Atom-by-atom nucleation and growth of graphene nanopores. *Proc. Natl. Acad. Sci. U.S.A.* **109**, 5953–5957 (2012).
23. G. He, S. Huang, L. F. Villalobos, M. T. Vahdat, M. D. Guiver, J. Zhao, W.-C. Lee, M. Mensi, K. V. Agrawal, Synergistic CO_2 -sieving from polymer with intrinsic microporosity masking nanoporous single-layer graphene. *Adv. Funct. Mater.* **30**, 2003979 (2020).
24. G. He, S. Huang, L. F. Villalobos, J. Zhao, M. Mensi, E. Oveisi, M. Rezaei, K. V. Agrawal, High-permeance polymer-functionalized single-layer graphene membranes that surpass the postcombustion carbon capture target. *Energ. Environ. Sci.* **12**, 3305–3312 (2019).
25. X. Wang, H. Dai, Etching and narrowing of graphene from the edges. *Nat. Chem.* **2**, 661–665 (2010).
26. A. Tracz, G. Wegner, J. P. Rabe, Scanning tunneling microscopy study of graphite oxidation in ozone-air mixtures. *Langmuir* **19**, 6807–6812 (2003).
27. X. Li, W. Cai, J. An, S. Kim, J. Nah, D. Yang, R. Piner, A. Velamakanni, I. Jung, E. Tutuc, S. K. Banerjee, L. Colombo, R. S. Ruoff, Large-area synthesis of high-quality and uniform graphene films on copper foils. *Science* **324**, 1312–1314 (2009).
28. M. Rezaei, S. Li, S. Huang, K. V. Agrawal, Hydrogen-sieving single-layer graphene membranes obtained by crystallographic and morphological optimization of catalytic copper foil. *J. Membr. Sci.* **612**, 118406 (2020).

29. S. Huang, M. Dakhchoune, W. Luo, E. Oveisi, G. He, M. Rezaei, J. Zhao, D. T. L. Alexander, A. Züttel, M. S. Strano, K. V. Agrawal, Single-layer graphene membranes by crack-free transfer for gas mixture separation. *Nat. Commun.* **9**, 2632 (2018).
30. P. R. Kidambi, G. D. Nguyen, S. Zhang, Q. Chen, J. Kong, J. Warner, Facile fabrication of large-area atomically thin membranes by direct synthesis of graphene with nanoscale porosity. *Adv. Mat.* **30**, 1804977 (2018).
31. A. Eckmann, A. Felten, A. Mishchenko, L. Britnell, R. Krupke, K. S. Novoselov, C. Casiraghi, Probing the nature of defects in graphene by Raman spectroscopy. *Nano Lett.* **12**, 3925–3930 (2012).
32. A. C. Ferrari, D. M. Basko, Raman spectroscopy as a versatile tool for studying the properties of graphene. *Nat. Nanotechnol.* **8**, 235–246 (2013).
33. J.-L. Li, K. N. Kudin, M. J. McAllister, R. K. Prud'homme, I. A. Aksay, R. Car, Oxygen-driven unzipping of graphitic materials. *Phys. Rev. Lett.* **96**, 176101 (2006).
34. Y. Mulyana, M. Uenuma, Y. Ishikawa, Y. Uraoka, Reversible oxidation of graphene through ultraviolet/ozone treatment and its nonthermal reduction through ultraviolet irradiation. *J. Phys. Chem. C* **118**, 27372–27381 (2014).
35. T. Sun, S. Fabris, Mechanisms for oxidative unzipping and cutting of graphene. *Nano Lett.* **12**, 17–21 (2012).
36. F. Raffone, F. Savazzi, G. Cicero, Controlled pore generation in single-layer graphene oxide for membrane desalination. *J. Phys. Chem. Lett.* **10**, 7492–7497 (2019).
37. A. M. Suarez, L. R. Radovic, E. Bar-Ziv, J. O. Sofo, Gate-voltage control of oxygen diffusion on graphene. *Phys. Rev. Lett.* **106**, 146802 (2011).
38. G. Lee, B. Lee, J. Kim, K. Cho, Ozone adsorption on graphene: Ab initio study and experimental validation. *J. Phys. Chem. C* **113**, 14225–14229 (2009).
39. L. F. Villalobos, S. Huang, M. Dakhchoune, G. He, W.-C. Lee, K. V. Agrawal, Polybenzimidazole copolymer derived lacey carbon film for graphene transfer and contamination removal strategies for imaging graphene nanopores. *Carbon* **173**, 980–988 (2021).
40. A. Govind Rajan, K. S. Silmore, J. Swett, A. W. Robertson, J. H. Warner, D. Blankschtein, M. S. Strano, Addressing the isomer cataloguing problem for nanopores in two-dimensional materials. *Nat. Mater.* **18**, 129–135 (2019).
41. X. Chu, L. D. Schmidt, Reactions of NO, O_2, H_2O, and CO_2 with the basal plane of graphite. *Surf. Sci.* **268**, 325–332 (1992).
42. R. T. Yang, C. Wong, Kinetics and mechanism of oxidation of basal plane on graphite. *J. Chem. Phys.* **75**, 4471–4476 (1981).
43. L. M. Robeson, The upper bound revisited. *J. Membr. Sci.* **320**, 390–400 (2008).
44. L. Xu, M. Rungta, J. Hessler, W. Qiu, M. Brayden, M. Martinez, G. Barbay, W. J. Koros, Physical aging in carbon molecular sieve membranes. *Carbon* **80**, 155–166 (2014).
45. Y. Yang, X. Yang, L. Liang, G. Yuyuan, H. Cheng, Large-area graphene-nanomesh/carbon-nanotube hybrid membranes for ionic and molecular nanofiltration. *Science* **364**, 1057–1062 (2019).
46. P. Cheng, M. M. Kelly, N. K. Moehring, W. Ko, A. P. Li, J. C. Idrobo, M. S. H. Boutilier, P. R. Kidambi, Facile size-selective defect sealing in large-area atomically thin graphene membranes for sub-nanometer scale separations. *Nano Lett.* **20**, 5951–5959 (2020).
47. A. W. Hauser, J. Schrier, P. Schwerdtfeger, Helium tunneling through nitrogen-functionalized graphene pores: Pressure- and temperature-driven approaches to isotope separation. *J. Phys. Chem. C* **116**, 10819–10827 (2012).
48. A. Razmjou, M. Asadnia, E. Hosseini, A. Habibnejad Korayem, V. Chen, Design principles of ion selective nanostructured membranes for the extraction of lithium ions. *Nat. Commun.* **10**, 5793 (2019).
49. K. A. Thompson, R. Mathias, D. Kim, J. Kim, N. Rangnekar, J. R. Johnson, S. J. Hoy, I. Bechis, A. Tarzia, K. E. Jelfs, B. A. McCool, A. G. Livingston, R. P. Lively, M. G. Finn, *N*-Aryl–linked spirocyclic polymers for membrane separations of complex hydrocarbon mixtures. *Science* **369**, 310–315 (2020).
50. A. J. Strudwick, N. E. Weber, M. G. Schwab, M. Kettner, R. T. Weitz, J. R. Wünsch, K. Müllen, H. Sachdev, Chemical vapor deposition of high quality graphene films from carbon dioxide atmospheres. *ACS Nano* **9**, 31–42 (2015).
51. S. Bae, H. Kim, Y. Lee, X. Xu, J.-S. Park, Y. Zheng, J. Balakrishnan, T. Lei, H. R. Kim, Y. I. Song, Y.-J. Kim, K. S. Kim, B. Özyilmaz, J.-H. Ahn, B. H. Hong, S. Iijima, Roll-to-roll production of 30-inch graphene films for transparent electrodes. *Nat. Nanotechnol.* **5**, 574–578 (2009).
52. C. Gong, H. C. Floresca, D. Hinojos, S. McDonnell, X. Qin, Y. Hao, S. Jandhyala, G. Mordi, J. Kim, L. Colombo, R. S. Ruoff, M. J. Kim, K. Cho, R. M. Wallace, Y. J. Chabal, Rapid selective etching of PMMA residues from transferred graphene by carbon dioxide. *J. Phys. Chem. C* **117**, 23000–23008 (2013).
53. Ç. Ö. Girit, J. C. Meyer, R. Erni, M. D. Rossell, C. Kisielowski, L. Yang, C. H. Park, M. F. Crommie, M. L. Cohen, S. G. Louie, A. Zettl, Graphene at the edge: Stability and dynamics. *Science* **323**, 1705–1708 (2009).
54. I. Horcas, R. Fernández, J. M. Gómez-Rodríguez, J. Colchero, J. Gómez-Herrero, A. M. Baro, WSXM: A software for scanning probe microscopy and a tool for nanotechnology. *Rev. Sci. Instrum.* **78**, 013705 (2007).
55. P. Giannozzi, S. Baroni, N. Bonini, M. Calandra, R. Car, C. Cavazzoni, D. Ceresoli, G. L. Chiarotti, M. Cococcioni, I. Dabo, A. Dal Corso, S. De Gironcoli, S. Fabris, G. Fratesi, R. Gebauer, U. Gerstmann, C. Gougoussis, A. Kokalj, M. Lazzeri, L. Martin-Samos, N. Marzari, F. Mauri, R. Mazzarello, S. Paolini, A. Pasquarello, L. Paulatto, C. Sbraccia, S. Scandolo, G. Sclauzero, A. P. Seitsonen, A. Smogunov, P. Umari, R. M. Wentzcovitch, QUANTUM ESPRESSO: A modular and open-source software project for quantum simulations of materials. *J. Phys. Condens. Matter.* **21**, 395502 (2009).
56. P. Giannozzi, O. Andreussi, T. Brumme, O. Bunau, M. B. Nardelli, M. Calandra, R. Car, C. Cavazzoni, D. Ceresoli, M. Cococcioni, N. Colonna, I. Carnimeo, A. D. Corso, S. de Gironcoli, P. Delugas, R. A. DiStasio, A. Ferretti, A. Floris, G. Fratesi, G. Fugallo, R. Gebauer, U. Gerstmann, F. Giustino, T. Gorni, J. Jia, M. Kawamura, H.-Y. Ko, A. Kokalj, E. Küçükbenli, M. Lazzeri, M. Marsili, N. Marzari, F. Mauri, N. L. Nguyen, H.-V. Nguyen, A. Otero-de-la-Roza, L. Paulatto, S. Poncé, D. Rocca, R. Sabatini, B. Santra, M. Schlipf, A. P. Seitsonen, A. Smogunov, I. Timrov, T. Thonhauser, P. Umari, N. Vast, X. Wu, S. Baroni, Advanced capabilities for materials modelling with QUANTUM ESPRESSO. *J. Phys. Condens. Matter.* **29**, 465901 (2017).
57. K. Lejaeghere, G. Bihlmayer, T. Björkman, P. Blaha, S. Blügel, V. Blum, D. Caliste, I. E. Castelli, S. J. Clark, A. Dal Corso, S. De Gironcoli, T. Deutsch, J. K. Dewhurst, I. Di Marco, C. Draxl, M. Dułak, O. Eriksson, J. A. Flores-Livas, K. F. Garrity, L. Genovese, P. Giannozzi, M. Giantomassi, S. Goedecker, X. Gonze, O. Grånäs, E. K. U. Gross, A. Gulans, F. Gygi, D. R. Hamann, P. J. Hasnip, N. A. W. Holzwarth, D. Iuşan, D. B. Jochym, F. Jollet, D. Jones, G. Kresse, K. Koepernik, E. Küçükbenli, Y. O. Kvashnin, I. L. M. Locht, S. Lubeck, M. Marsman, N. Marzari, U. Nitzsche, L. Nordström, T. Ozaki, L. Paulatto, C. J. Pickard, W. Poelmans, M. I. J. Probert, K. Refson, M. Richter, G. M. Rignanese, S. Saha, M. Scheffler, M. Schlipf, K. Schwarz, S. Sharma, F. Tavazza, P. Thunström, A. Tkatchenko, M. Torrent, D. Vanderbilt, M. J. Van Setten, V. Van Speybroeck, J. M. Wills, J. R. Yates, G. X. Zhang, S. Cottenier, Reproducibility in density functional theory calculations of solids. *Science* **351**, aad3000 (2016).
58. G. Prandini, A. Marrazzo, I. E. Castelli, N. Mounet, N. Marzari, Precision and efficiency in solid-state pseudopotential calculations. *npj Comput. Mater.* **4**, 72 (2018).
59. K. Lee, É. D. Murray, L. Kong, B. I. Lundqvist, D. C. Langreth, Higher-accuracy van der Waals density functional. *Phys. Rev. B - Condens. Matter Mater. Phys.* **82**, 081101 (2010).
60. P. Hollins, J. Pritchard, Interactions of CO molecules adsorbed on Cu(111). *Surf. Sci.* **89**, 486–495 (1979).
61. H. Marsh, E. O'Hair, R. Reed, W. F. Wynne-Jones, Reaction of atomic oxygen with carbon. *Nature* **198**, 1195–1196 (1963).
62. K. Xu, P. D. Ye, Theoretical study on the oxidation mechanism and dynamics of the zigzag graphene nanoribbon edge by oxygen and ozone. *J. Phys. Chem. C* **118**, 10400–10407 (2014).
63. C. Y. Pan, Gas separation by permeators with high-flux asymmetric membranes. *AIChE J.* **29**, 545–552 (1983).
64. Y. Shindo, T. Hakuta, H. Yoshitome, H. Inoue, Calculation methods for multicomponent gas separation by permeation. *Sep. Sci. Technol.* **20**, 445–459 (1985).
65. E. S. Rubin, Understanding the pitfalls of CCS cost estimates. *Int. J. Greenh. Gas Control.* **10**, 181–190 (2012).
66. L. S. White, K. D. Amo, T. Wu, T. C. Merkel, Extended field trials of Polaris sweep modules for carbon capture. *J. Membr. Sci.* **542**, 217–225 (2017).
67. S. Wang, Y. Xie, G. He, Q. Xin, J. Zhang, L. Yang, Y. Li, H. Wu, Y. Zhang, M. D. Guiver, Z. Jiang, Graphene oxide membranes with heterogeneous nanodomains for efficient CO_2 separations. *Angew. Chemie - Int. Ed.* **56**, 14246–14251 (2017).
68. M. Karunakaran, L. F. Villalobos, M. Kumar, R. Shevate, F. H. Akhtar, K. V. Peinemann, Graphene oxide doped ionic liquid ultrathin composite membranes for efficient CO_2 capture. *J. Mater. Chem. A* **5**, 649–656 (2017).
69. H. W. Kim, H. W. Yoon, S. Yoon, B. M. Yoo, B. K. Ahn, Y. H. Cho, H. J. Shin, H. Yang, U. Paik, S. Kwon, Selective gas transport through few-layered graphene and graphene oxide membranes. *Science* **342**, 91–95 (2013).
70. F. Zhou, H. N. Tien, W. L. Xu, J. T. Chen, Q. Liu, E. Hicks, M. Fathizadeh, S. Li, M. Yu, Ultrathin graphene oxide-based hollow fiber membranes with brush-like CO_2-philic agent for highly efficient CO_2 capture. *Nat. Commun.* **8**, 2107 (2017).
71. Y. Fu, Y. B. Jiang, D. Dunphy, H. Xiong, E. Coker, S. Chou, H. Zhang, J. M. Vanegas, J. G. Croissant, J. L. Cecchi, S. B. Rempe, C. J. Brinker, Ultra-thin enzymatic liquid membrane for CO_2 separation and capture. *Nat. Commun.* **9**, 990 (2018).
72. T. J. Kim, H. Vrålstad, M. Sandru, M. B. Hägg, Separation performance of PVAm composite membrane for CO_2 capture at various pH levels. *J. Membr. Sci.* **428**, 218–224 (2013).
73. P. D. Sutrisna, J. Hou, M. Y. Zulkifli, H. Li, Y. Zhang, W. Liang, D. M. D'Alessandro, V. Chen, Surface functionalized UiO-66/Pebax-based ultrathin composite hollow fiber gas separation membranes. *J. Mater. Chem. A* **6**, 918–931 (2018).
74. P. D. Sutrisna, J. Hou, H. Li, Y. Zhang, V. Chen, Improved operational stability of Pebax-based gas separation membranes with ZIF-8: A comparative study of flat sheet and composite hollow fibre membranes. *J. Membr. Sci.* **524**, 266–279 (2017).

75. S. Kim, J. Hou, Y. Wang, R. Ou, G. P. Simon, J. G. Seong, Y. M. Lee, H. Wang, Highly permeable thermally rearranged polymer composite membranes with a graphene oxide scaffold for gas separation. *J. Mater. Chem. A* **6**, 7668–7674 (2018).
76. Q. Fu, J. Kim, P. A. Gurr, J. M. P. Scofield, S. E. Kentish, G. G. Qiao, A novel cross-linked nano-coating for carbon dioxide capture. *Energ. Environ. Sci.* **9**, 434–440 (2016).
77. K. Xie, Q. Fu, C. Xu, H. Lu, Q. Zhao, R. Curtain, D. Gu, P. A. Webley, G. G. Qiao, Continuous assembly of a polymer on a metal-organic framework (CAP on MOF): A 30 nm thick polymeric gas separation membrane. *Energ. Environ. Sci.* **11**, 544–550 (2018).
78. S. Li, Z. Wang, C. Zhang, M. Wang, F. Yuan, J. Wang, S. Wang, Interfacially polymerized thin film composite membranes containing ethylene oxide groups for CO_2 separation. *J. Membr. Sci.* **436**, 121–131 (2013).
79. J. M. P. Scofield, P. A. Gurr, J. Kim, Q. Fu, S. E. Kentish, G. G. Qiao, Development of novel fluorinated additives for high performance CO_2 separation thin-film composite membranes. *J. Membr. Sci.* **499**, 191–200 (2016).
80. S. Kim, S. H. Han, Y. M. Lee, Thermally rearranged (TR) polybenzoxazole hollow fiber membranes for CO_2 capture. *J. Membr. Sci.* **403–404**, 169–178 (2012).
81. Z. Qiao, S. Zhao, M. Sheng, J. Wang, S. Wang, Z. Wang, C. Zhong, M. D. Guiver, Metal-induced ordered microporous polymers for fabricating large-area gas separation membranes. *Nat. Mater.* **18**, 163–168 (2019).

Acknowledgments: We acknowledge the host institution EPFL for support. We also acknowledge B. C. Le Geyt for help with setting up LabVIEW. We thank M. Razaei and R. Padman for the photograph and the schematic of the setup. **Funding:** We thank GAZNAT for funding the project. Parts of the project were funded by Swiss National Science Foundation Assistant Professor Energy Grant (PYAPP2_173645), European Research Council Starting Grant (805437-UltimateMembranes), Swiss Competence Center of Energy Research–Efficiency of Industrial Processes (SCCER-EIP; phase 2), and Swiss National Supercomputing Center (production projects s860 and s953). **Author contributions:** K.V.A. and S.H. conceived the project and wrote the manuscript. S.H. built the MGR setup and carried out the membrane experiments. S.L. carried out STM experiments and related analysis. L.F.V. did the HRTEM and AC-HRTEM experiments and analyzed the pore structure. E.O. helped with AC-HRTEM experiments. M.D., D.J.B., and L.F.V. synthesized the large-area membranes. M.Me. helped with the XPS experiments. M.T.V. carried out the ab initio calculations on adsorption energy. M.Mi. performed the techno-economic analysis. All authors discussed the results and commented on the manuscript. **Competing interests:** K.V.A. and S.H. are inventors on a millisecond etching patent application related to this work filed by GAZNAT (no. EP20166877.9, filed 30 March 2020). K.V.A., D.J.B., and L.F.V. are inventors on a membrane fabrication patent application related to this work filed by EPFL (no. EP20174809.2, filed 14 May 2020). The authors declare that they have no other competing interests. **Data and materials availability:** All data needed to evaluate the conclusions in the paper are present in the paper and/or the Supplementary Materials. Additional data related to this paper may be requested from the authors.

Submitted 1 October 2020
Accepted 12 January 2021
Published 24 February 2021
10.1126/sciadv.abf0116

Citation: S. Huang, S. Li, L. F. Villalobos, M. Dakhchoune, M. Micari, D. J. Babu, M. T. Vahdat, M. Mensi, E. Oveisi, K. V. Agrawal, Millisecond lattice gasification for high-density CO_2- and O_2-sieving nanopores in single-layer graphene. *Sci. Adv.* **7**, eabf0116 (2021).

Science Advances

Millisecond lattice gasification for high-density CO_2- and O_2-sieving nanopores in single-layer graphene

Shiqi Huang, Shaoxian Li, Luis Francisco Villalobos, Mostapha Dakhchoune, Marina Micari, Deepu J. Babu, Mohammad Tohidi Vahdat, Mounir Mensi, Emad Oveisi and Kumar Varoon Agrawal

Sci Adv **7** (9), eabf0116.
DOI: 10.1126/sciadv.abf0116